Chinese Chemical Letters 33 (2022) 1895–1900

Contents lists available at ScienceDirect

Chinese Chemical Letters

journal homepage: www.elsevier.com/locate/cclet

# Metal-polyphenol-coordinated nanomedicines for Fe(II) catalyzed photoacoustic-imaging guided mild hyperthermia-assisted ferroustherapy against breast cancer

Xinying Yu[1], Tongyi Shang[1], Guodong Zheng, Hailong Yang, Yuwei Li, Yanjun Cai, Guoxi Xie*, Bin Yang*

*The Sixth Affiliated Hospital, Department of Biomedical Engineering, School of Basic Medical Sciences, Guangzhou Medical University, Guangzhou 511436, China*

ARTICLE INFO

*Article history:*
Received 9 August 2021
Revised 5 October 2021
Accepted 11 October 2021
Available online 16 October 2021

*Keywords:*
Ferroptosis
Metal-polyphenol nanomedicines
Fenton reaction
Mild hyperthermia
Photoacoustic imaging

ABSTRACT

Ferroustherapy has gained great attention for anti-cancer treatment in recent years. Enlightened by temperature-mediated Fenton reaction in industrial waste water removal, we designed a iron-based polyphenol-coordinated nanomedicines for mild hyperthermia-assisted anti-cancer ferroustherapy. In brief, Fe-GA@BSA nanoparticles was synthesized by self-assembly and sorafenib (SRF) was loaded into Fe-GA@BSA to establish Fe-GA@BSA-SRF nanomedicines. The result nanomedicines can induce ferroptosis in cancer cells by accelerating Fenton reaction. And the photothermal effect of Fe-GA@BSA-SRF was used for mild hyperthermia-assisted ferroustherapy. The nanomedicines performs good anti-cancer therapeutic efficacy by inducing the production of ROS and inhibiting glutathione peroxidase 4 (GPX4) expression *in vitro* and *in vivo*. Besides, the broad absorption of Fe-GA@BSA-SRF in near infrared region endows it with photoacoustic imaging ability. This study provides ideas about rational design on iron-based nanoparticles for anti-cancer ferroustherapy.



Ferroptosis is a new type pf programmed cell death with features of accumulative iron, increased reactive oxygen species (ROS) levels and lipid peroxidation products [1,2]. $Fe^{2+}$ catalyzes Fenton reaction and Haber-Weiss reaction to produce ROS and lipid peroxides thus results in mitochondrial dysfunction. On the other hand, some ferroptosis inducers inhibit the expression of glutathione peroxidase 4 (GPX4), a phospholipid hydroperoxidase reduces intracellular peroxides, hence lead to the occurrence of ferroptosis in some drug-resistant cancer cells [3–5]. Since ferroptosis bypasses cell resistance against apoptosis and reduces the multidrug resistance in tumor cells [6] therefore some recently developed anti-cancer strategies are designed to induce ferroptosis at tumor sites. In recent years, iron-based or ferroptosis inducer-loaded nanoparticles have been constructed and used to kill cancer cells [7]. They treat cancer cells by inducing Fenton reaction, depleting endogenous GSH, inhibiting GPX4 expression and increase intracellular peroxidative production [8–12]. However, the application of iron-based nanoparticles is limited by its high toxicity and low efficacy. It was reported that iron-based nanoparticles may inhibit tumor growth at a high dose (i.v. 75 mg/kg) which might cause toxicity and brings side effect in the body [13]. There is an urgent requirement to develop efficient ferroustherapy. Until recently, synergistic ferroustherapies have been developed in combination with chemotherapy [14,15], photodynamic therapy (PDT) [16–18], photothermal therapy (PTT) [19], starvation therapy [20] and immunotherapy [21–23]. Nevertheless, as a temperature-dependent reaction, the moderate elevation in temperature can accelerate Fenton reaction, thus produces more ROS. Therefore, ferroptosis shows its potential in combination with photothermal therapy for an enhanced anti-cancer therapeutic effect. Up to date, mild hyperthermia has been applied in anti-cancer treatment in combination with other therapeutic methods including but not limited to immunotherapy [24–26]. However, there are few reports about mild hyperthermia applied in ferroustherapy for synergistic tumor therapy.

Metal-polyphenol networks have gained attention from researchers for years owing to its simple fabrication, pH responsiveness, good stability and bioavailability. Polyphenolic compounds are naturally derivatives or artificially modified polymers or drugs [27]. The abundant phenol groups endows polyphenolic com-

* Corresponding authors.
*E-mail addresses:* guoxixie@163.com (G. Xie), bin.yang@gzhmu.edu.cn (B. Yang).
[1] These authors contribute equally to this work.

https://doi.org/10.1016/j.cclet.2021.10.021
1001-8417/

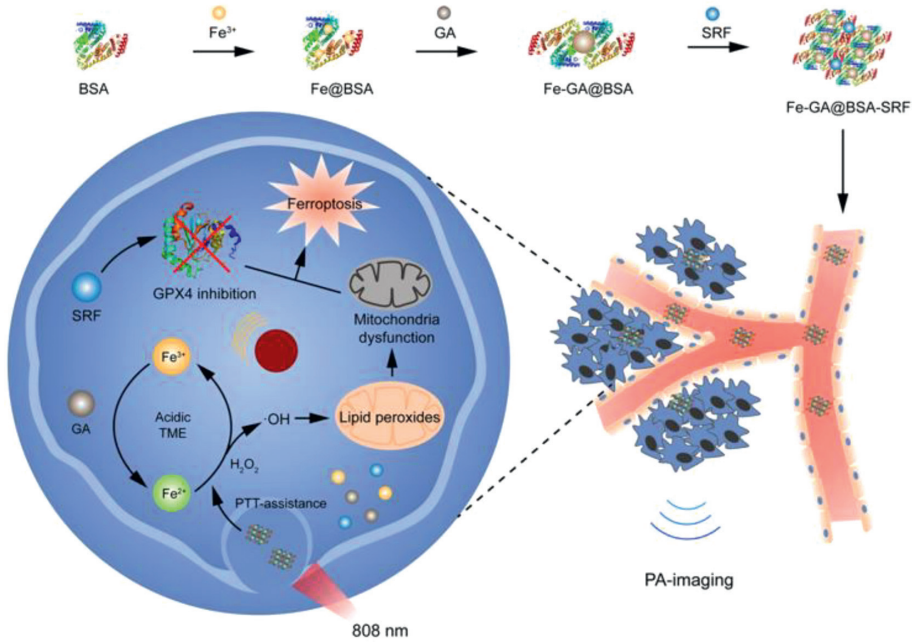


**Fig. 1.** Schematic illustration of PTT-assisted ferroustherapy and PA-imaging properties of Fe-GA@BSA-SRF (FGB-S). Iron-based polyphenol-coordinated nanomedicines FGB-S is synthesized by self-assembly and SRF-loading. After intravenous injection of FGB-S, the nanomedicines are internalized by tumor cells and disassemble in acidic tumor environment. $Fe^{3+}$ is reduced to $Fe^{2+}$ at the presence of GA and the result $Fe^{2+}$ promotes the production of ·OH by accelerating Fenton reaction. Then ·OH accumulation results in lipid peroxidation in mitochondria, which leads to mitochondrial dysfunction. On the other hand, the photothermal effect of FGB-S facilitates Fenton reaction in cancer cells. In combination of GPX4-inhibitive drug SRF, the nanomedicines performs good anti-cancer therapeutic efficacy. Besides, the photoacoustic imaging properties of FGB-S can make the treatment visualize.

pounds with reducibility and chelates with metal ions including $Fe^{3+}$, $Cu^{2+}$, $Gd^{3+}$ and $Zn^{2+}$ [28–31]. In recent years, metal-polyphenol networks have been applied to anti-cancer treatment including but not limited to photothermal, photodynamic and chemodynamic therapy, and imaging including computed tomography (CT) and magnetic resonance imaging (MRI) [32–35]. The versatility makes metal-polyphenol networks a promising theranostic agent for anti-cancer therapy.

Herein, we proposed a rational design of nanoparticles which consists of ferric ions, a naturally derived reductive polyphenol compound, gallic acid (GA), and a ferroptosis inducer, Sorafenib (SRF), to realize photothermal-assisted ferroustherapy for anti-cancer treatment (Fig. 1). The abundant phenol groups also allow GA to couple with transition metal ions $Fe^{3+}$ and form coordinate covalent bond. It is worth noting that, the number of coordination bonds decreases along with the decrease in pH which contributes to the disassembly of metal-polyphenol complexes [36]. After disassembly, $Fe^{3+}$ can be reduced to $Fe^{2+}$ by GA and initiates Fenton reaction to produce ROS under acidic condition at tumor site. The photothermal effect of the particles provides a mildly higher temperature which contributes to a faster rate of Fenton reaction and increases ROS production, thus induces more effective ferroptosis *in situ*. In addition, in participation of SRF the particles can induce GPX4 suppression at tumor site and the ROS is thus accumulated at tumor site. With its broad absorption in NIR region, Fe-GA@BSA appears to possess photoacoustic imaging function assisting therapy. A series of *in vitro* and *in vivo* experiments were conducted to examine the ferroptosis-inductive and anti-cancer efficacy of Fe-GA-SRF@BSA.

Detailed experimental procedures are described in Supporting information. We synthesized Fe-GA@BSA (FGB) by self-assembly of $Fe^{3+}$, gallic acid and BSA. And ferroptosis inducer sorafenib (SRF) was loaded onto FGB by stirring to obtain the nanomedicines. TEM images show that the Fe-GA@BSA-SRF (FGB-S) possessed a spherical morphology with the size of ~50 nm (Fig. 2A). AFM results demonstrate the height of FGB and FGB-S was 4 nm and 40 nm respectively (Fig. 2B and Fig. S1 in Supporting information). The hydrodynamic particle size of FGB-S is $88.06 \pm 8.42$ nm, which is slightly higher than the actual size of the particles (Fig. S2 in Supporting information). The variation of particle size was investigated by dynamic light scattering and the results show that particles size under different conditions was consistent to the size in pure water (Fig. S3 in Supporting information). And the size did not change significantly in water, PBS or culture medium within 7 days (Fig. S4 in Supporting information). The zeta potential of FGB-S was –27.7 mV. As shown in Fig. 2C, the increased absorbance of FGB-S at 265 nm suggests the loading of SRF and the concentration of Fe was determined to be 3.7 mmol/L by ICP-AES.

The release rate of SRF was studied under different pH (Fig. 2D). The results indicate a faster release rate of SRF at pH 5.5, which resembles tumor microenvironment and endocytic environment. The metal-coordination ability of GA varies at different pH and the weak stabilizing force at acidic environment accelerates the degradation of nanoparticles [37]. To investigate the photothermal effect of FGB, the solutions were irradiated by 808 nm laser and the variation in temperature was recorded. With a density of 1 W/cm$^2$, the temperature of 1 mmol/L FGB was raised by 35.8 °C (Fig. 2E). With a density of 0.5 or 0.3 W/cm$^2$, the temperature was raised by 12.6 °C (Fig. S5 in Supporting information) and 13 °C (Fig. S6 in Supporting information), respectively. After repeating the "irradiating-cooling" cycle for ten times, the photothermal effect of FGB did not attenuate (Fig. 2F). According to Ding's work [38], the photothermal conversion efficiency ($\eta$) was calculated by performing a "irradiating-cooling" cycle and the temperature was recorded at 10 s intervals (Fig. 2G) and system time constant was 417.6 s according to the 540 s cooling profile (Fig. 2H). As calculated, $\eta$ of FGB is 41.74%. The generation of ·OH *in vitro* was detected by MB degradation assay. The presence of ·OH can oxidize and degrade MB (Fig. S7 in Supporting information). The decrease in absorbance reflects MB degradation, which was up to 88% at

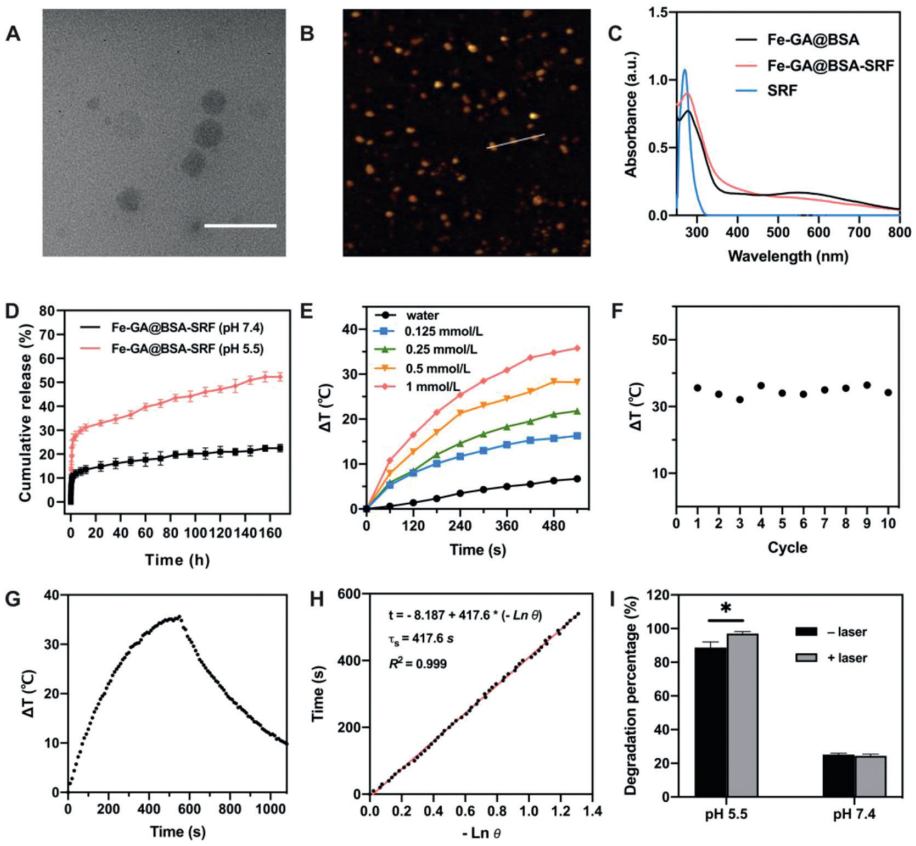


**Fig. 2.** (A) TEM image of FGB-S. Scale bar = 100 nm. (B) AFM result of FGB-S. (C) UV spectra of FGB, FGB-S and SRF. (D) Drug release of SRF under different conditions. (E) Temperature variation of FGB at different concentrations for 540 s (808 nm, 1 W/cm$^2$). (F) Temperature elevation of FGB (1 mmol/L) for ten cycles of "irradiation-cooling" for 1080 s each time (808 nm, 1 W/cm$^2$). (G) Temperature variation of FGB (1 mmol/L) in a "irradiation-cooling" cycle (808 nm, 1 W/cm$^2$). (H) Photothermal conversion of FGB (1 mmol/L) with 808 nm laser irradiation at 1 W/cm$^2$. (I) MB degradation rate of FGB with/without laser irradiation at different pH ($^*P < 0.05$).

pH 5.5 (Fig. 2I). After laser irradiation, the MB degradation was further elevated to 97%. Fenton-reaction has been applied to removal of industrial waste water due to its oxidization properties. It has been reported that an acidic environment and increased temperature can accelerate the reaction and improve the efficiency of nonylphenol ethoxylates removal [39]. Photothermal effect of FGB can induce a higher rate of Fenton-reaction by moderately elevation temperature *in situ*, which improves the production of $^{\bullet}$OH.

The cytotoxicity of FGB-S was examined in breast cancer cells and normal cells in comparison with free SRF. Comparing to free drug, FGB-S shows a higher toxicity in 4T1 cells and it was amplified after laser irradiation (Fig. 3A). For example, at the SRF concentration of 10 μmol/L, the cell viability was 34.5% for free SRF, 28% for FGB-S and 26% for FGB-S+NIR. To figure out how the particles induce cell death, a ferroptosis inhibitor Fer-1 and an apoptosis inhibitor Apo were used to co-culture cells with SRF, FGB-S. The cell viability was partially recovered after ferroptosis inhibitor Fer-1 or apoptosis inhibitor Apo treatment in FGB-S treated groups with or without laser (Fig. 3B). With the addition of Apo, relative cell viability of FGB-S treated cells recovered to 130%, which indicates that more cells experienced apoptosis rather than ferroptosis. However, the viability of cells in FGB-S+NIR group greatly recovered to 151% (Fer-1) and 141% (Apo), suggesting that cells experienced both apoptosis and ferroptosis. And the rate of ferroptosis significantly increased after laser irradiation. In normal cells (cos-7) FGB-S and FGB-S+NIR groups show a lower toxicity comparing to SRF group (Fig. 3C). The expression of GPX4 was studied in 4T1 cells after different treatments. First we studied the influence of FGB-S in comparison with SRF alone and found that FGB-S significantly suppressed the expression of GPX4 (Figs. S8 and S9 in Supporting information). Then we carried another experiment to investigate whether FGB has effects on GPX4. As shown in Fig. 3D and Fig. S10 (Supporting information), FGB can slightly down-regulate GPX4 expression while FGB-S shows stronger suppressive effect. And the co-incubation of FGB-S and Fer-1 partially reverse the suppressive effect on GPX4 expression. Western blotting results suggest that nanoparticles can suppress GPX4 expression with or without SRF and this can be reverted by ferroptosis inhibitor.

To detect the *in vitro* generation of ROS, a commercial probe DCFH-DA was used. It can be oxidized by free radicals and generate 2′,7′-dichlorofluorescein (DCF) with green fluorescence. In Fig. 4A, cells simply treated with acid or $H_2O_2$ did not trigger the boost of ROS generation. After adding FGB, stronger fluorescence was observed in cells and the positive cells increased up to 79.7% (Figs. S11 and S12 in Supporting information). But the FGB-S group showed less stronger fluorescence which may be due to the high toxicity of SRF. In addition, laser irradiation can also trigger the generation of ROS. After 808 nm laser irradiation, the production of ROS was significantly elevated (Figs. 4B and C, Fig. S13 in Supporting information). The results evidence that FGB may cause the increase in ROS production and the PTT-effect further enhance the generation of ROS.

The generated ROS does not remain in cells for good, it further attacks polyunsaturated fatty acids in mitochondrial membranes by generating lipid peroxides and leads to mitochondrial membrane dysfunction [40,41]. We used BODIPY$^{581/591}$-C11 to detect lipid peroxides, as its excitation wavelength will shift after oxidization by lipid peroxides. In Fig. 4D, the prevalence of green fluorescence in cells treated with FGB/FGB-S + $H_2O_2$ + pH 5.5 indicates a higher

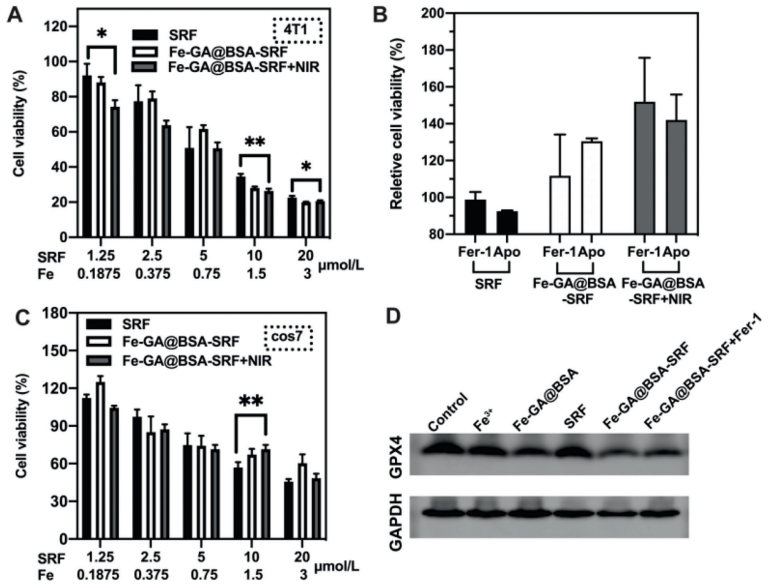


**Fig. 3.** (A) Cytotoxicity of SRF and FGB-S with/without laser irradiation (808 nm, 1 W/cm$^2$) in 4T1 cells for 24 h (*$P < 0.05$, **$P < 0.01$). (B) Cytotoxicity of SRF and FGB-S with/without laser irradiation (808 nm, 1 W/cm$^2$) at the presence of different inhibitors in 4T1 cells for 24 h. (C) Cytotoxicity of SRF and FGB-S with/without laser irradiation (808 nm, 1 W/cm$^2$) in cos7 cells for 24 h (**$P < 0.01$). (D) Expression of GPX4 in 4T1 cells with different treatment for 24 h.

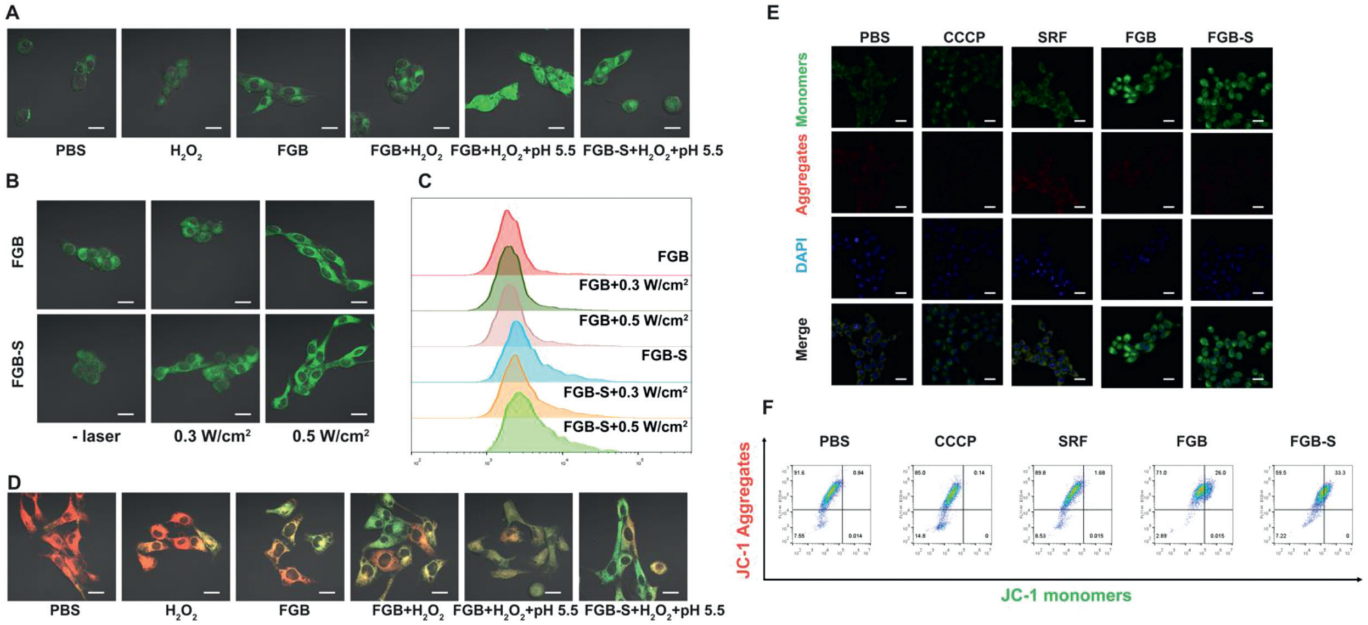


**Fig. 4.** (A) CLSM images of DCFH-DA assay detecting intracellular ROS level of 4T1 cells after various treatments. (B, C) CLSM images and flow cytometry results of DCFH-DA assay detecting intracellular ROS level of 4T1 cells treated with FGB-S and FGB with/without laser irradiation. (D) CLSM images of BODIPY$^{581/591}$-C11 assay detecting lipid peroxides of 4T1 cells after various treatments. (E, F) CLSM images and flow cytometry of JC-1 assay detecting mitochondrial membrane potential of 4T1 cells after various treatments. Scale bar = 20 μm.

amount of lipid peroxides in these groups. Oxidized BODIPY$^{581/591}$-C11 probe with green fluorescence suggests high concentration of ROS in cells, especially in membranes. Overwhelming ROS tends to attack unsaturated fatty in cell membranes and form lipid peroxides. Lipid oxidization may cause a lot of problems and mitochondria dysfunction is one of them. Lipid peroxides alters $\Delta\psi$m and the changes in $\Delta\psi$m influence functional metabolic status thus result in mitochondrial dysfunction. Variation in $\Delta\psi$m can be investigated by JC-1 probes. As shown in Fig. 4E, increased JC-1 monomers suggest the lower $\Delta\psi$m in cells which is a key signal of mitochondria dysfuntion. The flow cytometry results also reflect the decrease in $\Delta\psi$m after FGB and FGB-S treatment (Fig. 4F). Collectively, FGB and FGB-S induce disorder in cancer cells by a series of events, including ROS production, lipid peroxidation, $\Delta\psi$m variation and mitochondrial membrane dysfunction.

Since FGB has a wide absorption from 250 nm to 800 nm and a high absorbance in NIR region, it appears to be a good contrast agent for PA imaging. The PA spectrum of FGB showed a peak of absorbance at 690 nm, which was used for further PA-imaging. The animal experiments were performed according to the guidelines of the Animal Ethics Committee of Guangzhou Medical University. 4T1 tumor-bearing mouse received intravenous injection of

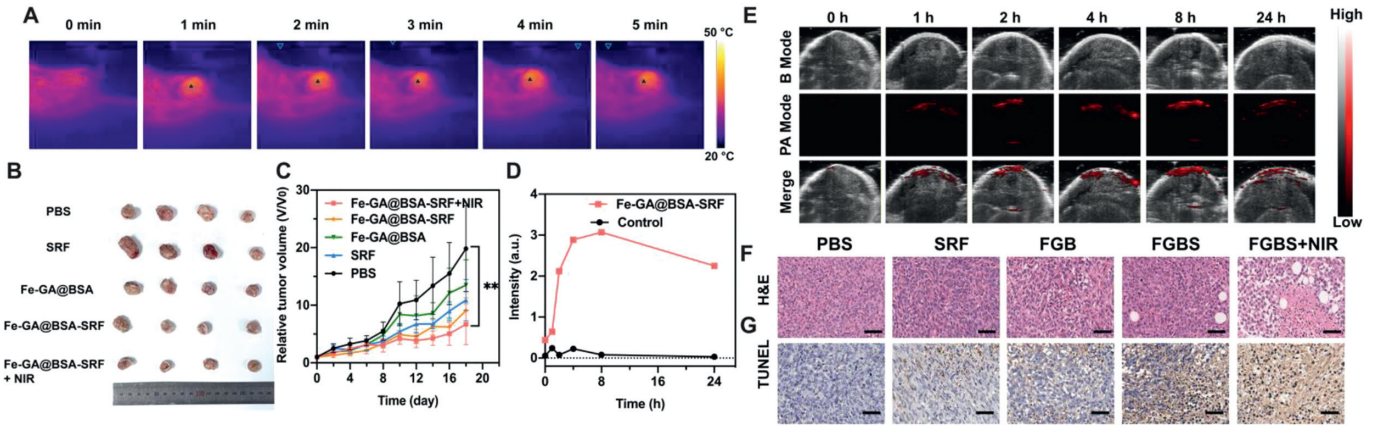


**Fig. 5.** (A) Temperature variation of mice at tumor site with laser irradiation at a density of 0.5 W/cm$^2$ for 5 min, 8 h-post injection of FGB-S. (B) Images of 4T1 tumors from different groups. (C) Tumor growth of 4T1 tumors in different groups (**$P < 0.01$). (D) PA signal intensities at tumor site post-injection. (E) PA images at tumor site post-injection. (F) H&E staining of 4T1 tumors from different groups. (G) TUNEL staining of 4T1 tumors from different groups. Scale bar = 50 μm.

200 μL FGB-S (Fe: 3.7 mmol/L) to investigate *in vivo* PA imaging. The PA signal at tumor site was recorded at different time intervals post-injection. The signal increased rapidly from 0 h-post injection to 4 h-post injection and reached maximum at 8 h-post injection (Figs. 5D and E). After 24 h, PA signal attenuated a little which indicates the retention of FGB-S at tumor site. The PA imaging properties of FGB-S indicates the potency of PA-guided therapeutic applications.

A 4T1 tumor-bearing model was chosen to examine the anti-cancer efficacy of FGB-S *in vivo*. Once the tumor volume reached ~100 mm$^3$, the mice were randomly allocated into 5 groups and intravenously injected with 100 μL of PBS, free SRF, FGB and FGB-S. The treatment was operated with a single dose of free drug or nanoparticles (SRF: 2 mg/mL; Fe: 3.7 mmol/L) at day 0 and 0.5 W/cm$^2$ laser irradiation 8 h-post injection for 5 min. The local temperature was elevated to 38.6 °C after irradiation (Fig. 5A). Comparing to PBS group, free SRF showed little anti-cancer efficacy and so did FGB group (Fig. 5B). Nonetheless, the combination of FGB and SRF showed a better inhibition on tumor growth and the introduction of moderate laser irradiation further enhanced its anti-cancer efficacy. The 0.5 W/cm$^2$ irradiation slightly increased the local temperature at tumor site, which accelerate *in-situ* Fenton-reaction and higher reaction rate brought more $^{\bullet}$OH and therefore damaged the function of cancer cells. At day 18, relative tumor volume of FGB-S+NIR group was significantly lower than control group ($P < 0.01$, Fig. 5C) which reflects the slower growth rate of tumor. It evidenced the elevated effect of FGB-S by slightly increased local temperature.

The main organs and tumor were harvested for H&E staining. The results showed that the treatment did not cause damages in heart, liver spleen and kidney (Fig. S14 in Supporting information). However, we found obvious metastasis in lung from PBS and FGB groups, while little or no metastasis occurs in other groups (Fig. S15 in Supporting information). Breast cancer is greatly aggressive with a high probability of lung metastasis occurrence which involves chemokine (C–C motif) ligand 2 (CCL2)-mediated inflammatory monocytes recruitment. In this study, the occurrence of lung metastasis decreased with the participation of SRF treatment. And some cavities were found in tumors from FGB-S and FGB-S+NIR groups, which is a sign of cancer cell death (Fig. 5F). The tumors were also subjected to TUNEL staining and tumor cells from FGB-S+NIR group were found to be highly apoptotic comparing to control group (Fig. 5G). This finding is consistent with the conclusion that FGB-S caused cell death partially by apoptosis. At the end of animal experiment, there was negligibly significant difference in body weights among these groups (Fig. S16 in Supporting information).

We have constructed ferric-coordinated polyphenol nanoparticles for triggering PTT-assisted ferroustherapy for anti-cancer treatment. A mild increase in temperature endows faster Fenton-reaction and Haber-Weiss reaction *in situ*. The role which GA plays in this nanomedicine is more than a reductant for ferrous supply, and it is also a switch for acidity-responsive degradation and drug release. We tested the production of ROS *in vitro* and examined the impact of excessive ROS on biological membranes and mitochondrial function. The results indicate the peroxidation of biological membranes and alteration in mitochondrial membrane potential, thus verified the damages in mitochondrial function. In combination with Sorafenib, the nanomedicine significantly suppressed GPX4 expression. The recovery in cell viability after treatment with different inhibitors suggests that the nanomedicine induced both apoptosis and ferroptosis in 4T1 cells. More importantly, the rate of ferroptosis increased significantly after NIR irradiation. It is noteworthy that the PTT effect of FGB amplified the production of ROS with a moderate hyperthermia by controlling the time and intensity of NIR irradiation, which avoids painful ambustion. In animal experiment the mild hyperthermia-assisted ferroustherapy showed higher anti-cancer effect comparing to using ferroustherapy alone, which has been proved by inhibitive tumor growth and higher apoptotic rate in tumor sites. Moreover, the photoacoustic effect of FGB can facilitate *in vivo* imaging of tumor during treatment. In summary, FGB-S nanoparticles provide a novel theranostic strategy based on ferroptosis and photoacoustic imaging. It is expected that FGB-S may benefit the development and application of anti-cancer nanoparticles in the future.

## Declaration of competing interest

The authors declare that they have no known competing financial interests or personal relationships that could have appeared to influence the work reported in this paper.

## Acknowledgments

This work was supported by grants from the National Natural Science Foundation of China (No. 51903062), Guangdong Basic and Applied Basic Research Foundation (No. 2020A1515011320), Science and Technology Projects of Guangzhou (No. 202102020757) and Subject Construction Project of Ba-

sic Medical Sciences of Guangzhou Medical University (Nos. JCXKJS2021B07, JCXKJS2021D09).

## Supplementary materials

Supplementary material associated with this article can be found, in the online version, at doi:10.1016/j.cclet.2021.10.021.

## References

[1] S.J. Dixon, K.M. Lemberg, M.R. Lamprecht, et al., Cell 149 (2012) 1060–1072.
[2] Y. Xie, W. Hou, X. Song, et al., Cell Death Differ. 23 (2016) 369–379.
[3] M.J. Hangauer, V.S. Viswanathan, M.J. Ryan, et al., Nature 551 (2017) 247–250.
[4] W.H. Koppenol, J. Butler, J.W. Leeuwen, Photochem. Photobiol. 28 (1978) 655–658.
[5] M.J. Burkitt, B.C. Gilbert, Free Radic. Res. Commun. 10 (1990) 265–280.
[6] J.M. Brown, L.D. Attardi, Nat. Rev. Cancer 5 (2005) 231–237.
[7] S. Wang, H. Liao, F. Li, D. Ling, Chin. Chem. Lett. 30 (2019) 847–852.
[8] T. Liu, W. Liu, M. Zhang, et al., ACS Nano 12 (2018) 12181–12192.
[9] Z. Shen, T. Liu, Y. Li, et al., ACS Nano 12 (2018) 11355–11365.
[10] S. Wang, F. Li, R. Qiao, et al., ACS Nano 12 (2018) 12380–12392.
[11] Q. Guan, R. Guo, S. Huang, et al., J. Control. Release 320 (2020) 392–403.
[12] J. Zhu, P. Dai, F. Liu, et al., Nano Lett. 20 (2020) 6235–6245.
[13] C. Zhang, W. Bu, D. Ni, et al., Angew. Chem. Int. Ed. 55 (2016) 2101–2106.
[14] G. Chen, Y. Yang, Q. Xu, et al., Nano Lett. 20 (2020) 8141–8150.
[15] Y. Yang, Y. Yu, H. Chen, et al., ACS Nano 14 (2020) 13536–13547.
[16] F. Xiao, B. Cao, L. Wen, et al., Chin. Chem. Lett. 31 (2020) 2516–2519.
[17] L. Yu, Z. Wang, Z. Mo, et al., Acta Pharm. Sin. B 11 (2021) 2004–2015.
[18] W. Ma, S. Sha, P. Chen, et al., Adv. Healthc. Mater. 9 (2020) 1901100.
[19] X. Liu, Y. Yang, M. Ling, et al., Adv. Func. Mater. 31 (2021) 2101709.
[20] X. Zhang, C. He, Y. Chen, et al., Biomaterials 275 (2021) 120987.
[21] Q. Jiang, K. Wang, X. Zhang, et al., Small 16 (2020) 2001704.
[22] J. Huang, B. Yang, Y. Peng, et al., Adv. Func. Mater. 31 (2021) 2011171.
[23] T. Shang, X. Yu, S. Han, B. Yang, Biomater. Sci. 8 (2020) 5241–5259.
[24] Y. Li, L. He, H. Dong, et al., Adv. Sci. 5 (2018) 1700805.
[25] Y. Liu, P. Maccarini, G.M. Palmer, et al., Sci. Rep. 7 (2017) 8606.
[26] X. Huang, Y. Yin, M. Wu, W. Zan, Q. Yang, Chin. Chem. Lett. 30 (2019) 1335–1340.
[27] Y. Guo, Q. Sun, F.G. Wu, Y. Dai, X. Chen, Adv. Mater. 33 (2021) 2007356.
[28] J. Zeng, M. Cheng, Y. Wang, et al., Adv. Healthc. Mater. 5 (2016) 772–780.
[29] H. Cao, Z. Chen, H. Zheng, Y. Huang, Biosens. Bioelectron. 62 (2014) 189–195.
[30] J. Qin, G. Liang, Y. Feng, et al., Nanoscale 12 (2020) 6096–6103.
[31] N. Ninan, A. Forget, V.P. Shastri, N.H. Voelcker, A. Blencowe, ACS Appl. Mater. Inter. 8 (2016) 28511–28521.
[32] T. Liu, M. Zhang, W. Liu, et al., ACS Nano 12 (2018) 3917–3927.
[33] Z. Xu, X. Wang, X. Liu, et al., ACS Appl. Mater. Inter. 9 (2017) 39657–39671.
[34] L. Zhang, S. Wan, C. Li, et al., Nano Lett. 18 (2018) 7609–7618.
[35] W. Zhu, S. Liang, J. Wang, et al., J. Mater. Sci: Mater. Med. 28 (2017) 74.
[36] J. Guo, Y. Ping, H. Ejima, et al., Angew. Chem. Int. Ed. 53 (2014) 5546–5551.
[37] J. Zhou, Z. Lin, Y. Ju, et al., Acc. Chem. Res. 53 (2020) 1269–1278.
[38] X. Ding, C.H. Liow, M. Zhang, et al., J. Am. Chem. Soc. 136 (2014) 15684–15693.
[39] K. Cui, H. Yi, Z.J. Zhou, Q.F. Zhuo, Z.C. Xu, Environ. Eng. Sci. 31 (2014) 217–224.
[40] A. Bindoli, Free Radical Bio. Med. 5 (1988) 247–261.
[41] M. Xiao, H. Zhong, L. Xia, Y. Tao, H. Yin, Free Radical Bio. Med. 111 (2017) 316–327.